Mechanistic Insight into the Formation and Deposition of Conductive, Layered Metal–Organic Framework Nanocrystals

*Emma K. Ambrogi, Patrick Damacet, Robert M. Stolz, and Katherine A. Mirica**

Department of Chemistry, Burke Laboratory, Dartmouth College, Hanover, NH 03755, United States.

*Corresponding author email: Katherine.a.mirica@dartmouth.edu

KEYWORDS: Metal–organic frameworks, conductive 2D materials, self-assembly, nanoscale morphology, oxidants, formation rate, *in situ* ATR-FTIR spectroscopy

ABSTRACT: This paper describes the use of the layered conductive metal–organic framework (MOF) (nickel)$_3$-(hexahydroxytriphenylene)$_2$ [$Ni_3(HHTP)_2$] as a model system for understanding the process of self-assembly within this class of materials. We confirm and quantify experimentally the role of oxidant in the synthetic process. Monitoring the deposition of $Ni_3(HHTP)_2$ with *in-situ* infrared spectroscopy revealed that MOF formation is characterized by an initial induction period, followed by linear growth with respect to time. The presence and identity of oxidizing agents is critical for the coordination-driven self-assembly of these materials, and impacts both the length of the induction period and the observed rate of MOF growth. A large

excess of hydrogen peroxide results in a 2× increase in observed deposition rate ($9.6 \pm 6.8 \times 10^{-4}$ vs. $5.0 \pm 2.8 \times 10^{-4}$ min^{-1}) over standard reaction conditions, but leads to the formation of large, irregularly shaped particles. Slower deposition rates in the presence of oxygen favor the formation of uniformly sized nanorods ($98 \pm 38 \times 25 \pm 6$ nm). These quantitative insights into the mechanism of HHTP-based MOF formation provide valuable information about the fundamental aspects of coordination and polymerization that are critical for nanoscale crystal engineering of structure–property relationships in this class of materials.

INTRODUCTION

Conductive two-dimensional layered metal–organic frameworks (MOFs) are promising materials for electroanalysis,[1–5] energy storage,[6–9] and catalysis.[10–14] Their multifunctional properties, including high surface area,[7,10,15] electrical conductivity,[15,16] and unique chemical reactivity[11,17,18] have paved the way to a range of applications in chemical catalysis and sensing,[1,11–14,18,19] physics and electronics,[6,9,10,20–22] and biosensing and biomedical diagnostics.[1,5,18,23–26] At their core, these 2D layered conductive MOFs have a rich chemistry that stems from the flexible redox states of their components, their tunable morphology, and their incorporation of diverse elements, both inorganic[27–29] and organic.[30–35] The functional properties of these MOFs in particular are influenced by the morphology,[36] synthetic route,[37] and crystal facet,[4] all of which are tied together by a set of growth kinetics. However, attaining a deeper understanding of the mechanistic details of MOF growth poses a challenge due to poor solubility of the final materials and redox activity of both the MOF and its precursors. Consequently, typical methods for studying chemical kinetics and supramolecular binding interactions, such as nuclear magnetic resonance spectroscopy (NMR)[38,39] and isothermal titration calorimetry (ITC),[40,41] are

not easily adapted for studying the self-assembly of MOFs. The absence of fundamental insight into coordination-polymerization that governs the rate of the assembly of conductive MOFs from their molecular precursors into crystalline structures hinders strategic efforts in the molecular design of structure–property relationships, morphological control, and deposition into devices for this class of materials.

The multifunctional properties of these layered conductive MOFs are highly dependent on the molecular components of the material.[21,42–44] Intrinsically, aspects such as redox states of constituents, edge functionality of the nanocrystalline products, and the underlying structural constraints imposed by component parts can be challenging to untangle when studying the final products instead of the processes involved in formation. In the subclass of these MOFs based on the hexahydroxytriphenylene (HHTP) ligand, structural properties are closely tied to the identity of the metal node. Previously reported cobalt- and nickel-based HHTP MOFs form a bilayered structure, in which extended sheets alternate with an intercalated layer of HHTP-metal units (**Figure 1a**).[27] In $Ni_3(HHTP)_2$, X-ray photoelectron spectroscopy (XPS) has shown Ni^{2+} to be the dominant redox state.[42] By contrast, the copper-based HHTP MOF is not isostructural to the Ni and Co members, but favors an AAA slipped-parallel packing structure,[45] and has a mixed valency of Cu^{1+} and Cu^{2+} nodes.[42,46] Coordination of lanthanide metal ions with HHTP creates a 3D MOF, where Ln^{3+} ions force the HHTP layers closer together.[28] In contrast, recently reported structures of a Bi(HHTP) coordination polymer have unique corrugated sheet topologies[47,48] and a flexible structure that shifts between two forms depending on the presence of water in the pores.[47] Although these structural subtleties are well documented, with trends in the redox activity and coordination geometry of the metals being significant contributing factors, no systematic studies have provided molecular-level insight for why the metal-linker combination impacts the structure in this way.

Recent reports have demonstrated that the structure and morphology of MOFs, as well as differences in their component structure, can greatly influence their multifunctional properties.[4,36,42,49] A closer look at the mechanistic details of the self-assembly process is necessary to gain deeper insights into the questions that have surrounded this class of MOFs since their discovery. Despite the widely reported applications of 2D layered conductive MOFs, current understanding of the process leading from homogeneous solution-phase reactants to templated solid-state products is lacking. While seminal studies for layered COFs based on HHTP and boronate ester chemistry have yielded valuable insights that have become instrumental in the advancement of the fields of COF-based electronics and controlled crystal growth,[50,51] analogous information for 2D layered MOF materials is not yet available. Model complexes in solution have been used to study the redox and spin properties of HHTP MOFs,[52,53] but these studies do not provide information about MOF nucleation, growth, or deposition. The identification of a rate law for specific reagents has remained largely unexplored. For example, heterogeneous solvothermal methods of HHTP MOF synthesis typically utilize stoichiometric amounts or a slight excess of metal ions (2:1 M:HHTP or greater),[27,28,54,55] but the impact of these reaction conditions on the morphology and properties of the resulting MOF has not been systematically reported. Furthermore, heterogeneous, hydrothermal syntheses of triphenylene-based MOFs are almost universally run under ambient atmosphere,[49] yet the role of oxygen and/or oxidizing agents has not been systematically investigated. In particular, interfacial growth methods for HHTP MOFs, which can result in MOF thin films and/or highly oriented crystals, use directional reaction geometries, which likely serve to mediate the diffusion of oxygen to the reactants, but the role of oxygen has not been explicitly acknowledged.[56,57] Work recently published by our group and others found that control of oxidation state of the starting materials and control over oxidants in

the MOF formation reaction could provide control over epitaxial MOF alignment and morphology.[4,49] Understanding how 2D MOFs self-assemble is important to the strategic design of the structure–property relationships in this unique class of 2D materials.

This work presents the first systematic investigation of the formation and deposition of nanocrystalline $Ni_3(HHTP)_2$, a 2D layered conductive MOF. By carefully controlling the presence, identity, and concentration of oxidants, we determine the role of redox reactions in the formation process of MOFs, and the overall rates related to MOF growth and deposition onto substrates. Herein, we discover and present the initial stage of MOF formation that consists of a coordination stage coinciding with the spectroscopically observed induction time, followed by a period of linear growth vs. time that is limited by the oxidation state of reactive components. We attribute the formation processes and dependence on oxygen to the reactivity of different oxidation states of HHTP (See **Figure S1**). Our study systematically compares the use of several oxidizing agents, including free oxygen diffusion from air and the addition of H_2O_2. This investigation demonstrates the relationship between growth rates and oxidant concentration, and the correlation of rates with control over the nanoscale morphology of MOF crystals. Increasing the dissolved oxygen concentration by bubbling air through the reaction results in a 10-fold increase in observed rate over the reaction driven by passive diffusion of air, although both conditions yield samples with similar morphology. By contrast, adding an excess of H_2O_2 to the reaction further doubles the observed rate of MOF formation, but results in irregularly shaped MOF particles. The insights into the formation mechanism of this MOF have the potential to inform the incorporation of 2D MOF materials into functional devices.

EXPERIMENTAL DESIGN

Naming Conventions for Triphenylene-based MOFs: Since the initial reports of layered, conductive MOFs incorporating triphenylene-based linkers, a variety of naming conventions have been employed to describe these materials.[27,32,58] These include the form M-CAT-1 for hexahydroxytriphenylene MOFs (where M is the metal node linking HHTP), the form $M_3(HXTP)_2$, (where M is the metal node and X represents the heteroatom of the triphenylene-based linker), or the form M-HXTP using the same abbreviations. The $M_3(HXTP)_2$ form represents a stoichiometric formula for the coordinated 2D layer, and indicates the oxidation state of metal and linker in a charge-neutral layer: M^{2+} and $[HHTP]^{3-}$. For the cobalt- and nickel-hexahydroxytriphenylene analogs, which contain the intercalated layer, the total stoichiometric ratio for both layers is 9 Ni: 4 HHTP. However, it is important to recognize that neither the name $Cu_3(HHTP)_2$ nor the name $Ni_9(HHTP)_4$ reflect complete chemical formulas, as these names do not account for the presence of edge sites, defects, coordinated water, or trapped solvent molecules. In light of this inconsistency, we have adopted the naming convention of $M_3(HXTP)_2$ for all 2D layered triphenylene-based MOFs, regardless of packing mode, because this convention is the best descriptor for the connectivity of the MOF layer, and clearly indicates the structural commonalities between all the MOFs of this class.

Choice of MOF System: We chose $Ni_3(HHTP)_2$ as a model system for studying MOF formation and deposition *in situ* for several reasons: 1) the established utility of HHTP-based MOFs for applications such as chemical sensing and catalysis,[3,11] 2) the straightforward synthetic access of the components and starting materials, which has led to their use in many applications,[59] 3) the established demonstration that nanostructured control of interfaces has a profound influence on the functional performance of this class of materials,[4,21,36,60,61] and 4) the precedent for depositing $Ni_3(HHTP)_2$ on surfaces,[21,54,62–64] which is a critical feature for the method of spectroscopic

monitoring of MOF growth we employed. We modified the synthetic procedures slightly from previously published reaction conditions by lowering the temperature and changing the solvent from pure water to a 20:3 water:dimethylformamide (DMF) mixture, ensuring that all components could be dissolved, so that the reaction could proceed homogeneously (**Figure 1a**).

Choice of Spectroscopic Technique: We selected attenuated total reflectance Fourier transform infrared spectroscopy (ATR-FTIR) for *in situ* monitoring of MOF formation. ATR-FTIR is a powerful technique that relies on the generation of an evanescent wave adjacent to the surface of an optical crystal;[65,66] attenuation of the wave by chemical species near the crystal by absorbing, scattering, and reflecting infrared light leads to observable absorbance bands that correspond to specific vibrational modes of proximal chemical entities. The evanescent wave is most sensitive to the chemical environment within 2 μm of the surface of the ATR crystal with the sensitivity dropping exponentially with distance.[65,66] For this reason, IR sampling of reactions by ATR methods are well suited to studies of the deposition of materials onto the ATR crystal. We constructed a custom reaction cell accessory in which reactions could be conducted, and we tracked the formation of MOF by monitoring the change in absorbance at three characteristic vibrational frequencies known to represent key structural features of the MOF (See Supporting Information, **Section IV**, for more details). Through a series of experiments, we assessed variables relevant to MOF formation controlling for the presence and concentration of oxidizing agents (O_2 or H_2O_2). We compared the results with bulk solution experiments through which we were able to monitor reaction yield, MOF crystallinity, and morphology. The interpretation of the spectroscopic results presented here relies on a key assumption: that the MOF particles deposited on the surface of the ATR crystal are similar in size and morphology to those collected from solution. We believe this to be a reasonable assumption based on previously reported $Ni_3(HHTP)_2$ hydrothermal surface

deposition methods where particles collected from solution are similar in morphology and particle size (within an order of magnitude) to those deposited on substrates.[26,54,67]

Choices of Reagents, Oxidants, and Experimental Conditions: As with all chemical reactions, many factors, including reaction temperature, pH, and the concentration of all reagents likely contribute to the overall observed rate of $Ni_3(HHTP)_2$ deposition. While all of these factors may be worthy of further study, we have chosen specifically to study the impact of the oxidant on $Ni_3(HHTP)_2$ deposition for the following reasons: Firstly, the role of the oxidant has been mentioned in previous reports of this material, but remains underexplored.[4,21,27,54,56,68–70] Despite this gap in the literature, we found that manipulating the introduction of oxidants into $Ni_3(HHTP)_2$ synthesis had a dramatic impact on MOF morphology and crystallinity, necessitating the understanding of this important reaction parameter before seeking to elucidate the impact of other reagents and conditions. In order to elucidate the role of oxidants, the concentrations of other reagents were held constant for all experiments. The 2:1 ratio of Ni^{2+} ions to HHTP linkers represents the standard ratio in reports of $Ni_3(HHTP)_2$,[4,42,54,62,64,68,69,71,72] and the use of 11.1 mM HHTP solution is similar to previously reported hydrothermal syntheses of these materials.[4,42,54] Additionally, the acetate salt is the most common nickel source used in $Ni_3(HHTP)_2$ syntheses,[4,23,42,54,55,62,64,68,69,71–74] as the acetate counter ion serves to modulate the pH of the reaction solution and assist in the deprotonation of HHTP, which is necessary for $Ni_3(HHTP)_2$ self-assembly. Two important changes from standard synthesis conditions were made in order to study MOF deposition *in situ*: firstly, a mixture of dimethylformamide (DMF) and water was used as the solvent matrix, rather than pure water, so that HHTP could be fully dissolved at the start of the reaction. We compared our samples with $Ni_3(HHTP)_2$ produced from a hydrothermal, heterogeneous control synthesis in order to ensure that the impact of this change was minimal.

Secondly, *in situ* ATR-FTIR measurements of reactions were carried out at room temperature rather than with applied heat, an experimental limitation of the current reaction cell. We made multiple comparisons between samples produced at room temperature vs. 85 °C in order to understand the impacts temperature might have on the self-assembly of this MOF.

RESULTS AND DISCUSSION

Impact of Oxidants in Bulk Syntheses. We began our investigation by examining the process of $Ni_3(HHTP)_2$ formation in bulk solution, and the effect of oxidizing agents on the transformation of HHTP into MOF. HHTP can exist in 7 possible oxidation states ranging from the fully oxidized tris-quinone (HHTP-tq) to the fully reduced tris-catecholate (HHTP-tc) (See **Figure S1**).[52,75,76] To ensure HHTP remained in a relatively reduced form prior to the start of the reaction, we synthesized and isolated HHTP in the absence of oxygen and degassed all solvents before beginning each MOF growth experiment (See Supporting Information, **Section II** for more details). The oxidation state of the HHTP starting material was assessed with electron paramagnetic resonance (EPR), NMR spectroscopy, and UV-vis spectroscopy (See **Figures S2-S5**) and shown to be relatively reduced compared with commercially available ligand, although the presence of carbon-centered radical character observed with EPR indicated the partially oxidized state of the ligand used in this study (See **Figure S5**). We examined the impact of oxidizing agents on the crystallinity and morphology of the resulting MOF particles using scanning electron microscopy (SEM) and powder X-ray diffraction (PXRD) shown in **Figure 1b-e**. For each of the conditions compared, **Figure 1** shows a photograph of the reaction after 1 hour, a representative SEM image of the MOF nanoscale morphology, and the PXRD pattern, compared with a simulated diffraction pattern based on ABAB layered structure of the previously reported

crystal structure for $Co_3(HHTP)_2$ (which is isostructural to $Ni_3(HHTP)_2$).[27] Miller indices of corresponding Bragg planes are indicated on the plot.

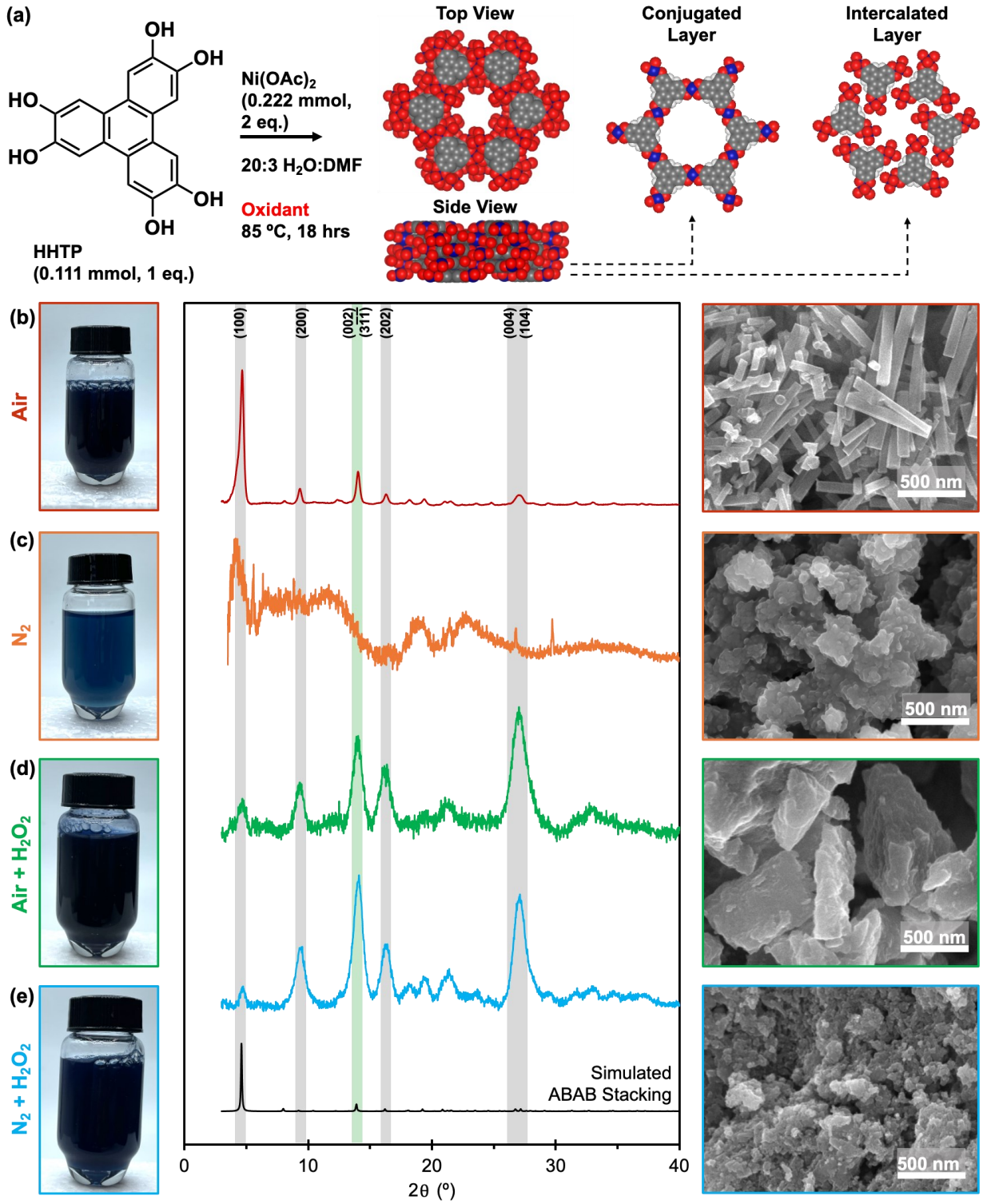

Figure 1. The impact of synthetic conditions on $Ni_3(HHTP)_3$ morphology, assessed by powder X-ray diffraction (PXRD), and scanning electron microscopy (SEM). **(a)** General synthetic conditions and structure of $Ni_3(HHTP)_2$, including conjugated and intercalated layers observed in the ABAB stacking pattern. **(b-e)** Four homogeneous synthetic conditions (in a 20:3 H_2O: DMF mixture) were compared: **(b)** bubbling air, **(c)** bubbling nitrogen, **(d)** added H_2O_2 (1 mL, 6% H_2O_2) while bubbling air and **(e)** added H_2O_2 (1 mL, 6% H_2O_2) while bubbling nitrogen. The normalized PXRD patterns (center), and representative SEM images (left) of each MOF sample are shown, as well as a photograph of the reaction vial after 1 hr of reaction time (right). See supporting information for additional SEM images and experimental details.

The presence of oxidizing agent was critical to MOF formation. Bubbling of oxygen through the reaction (while heating to 85 ° C) —either in a homogeneous reaction with reagents dissolved in a water/DMF mixture (**Figure 1b**) or in a hydrothermal reaction with reagents suspended in degassed water (**Figure S6**)— produced nanoscale rods, as characterized by SEM. In PXRD analysis, the (100) peak of these samples is particularly prominent, as were key peaks corresponding to the presence of the intercalated layer, including the (002)/ $(3\bar{1}\bar{1})$ peak at 14° 2θ (highlighted in green in **Figure 1,** see **Figure S7** and **Table S1** for more details). Crystallinity, morphology, and conductivity (see **Table S2**) generally aligned well with previous reports of this material,[27,42,54,56,61] as did the simulated diffraction pattern generated from the single crystal x-ray structure of the isostructural $Co_3(HHTP)_2$ MOF reported by Hmadeh et al.[27] In contrast, the absence of oxygen (**Figure 1c**) suppressed MOF formation, as evidenced in the low intensity of characteristic MOF peaks by PXRD, and the lack of visible reaction after 1 hr (**Figure S8**). The addition of excess H_2O_2 (16 eq., 1 mL 6% H_2O_2) to the reaction, with or without bubbled air,

produced visible solids in the reaction vial after 1 hr, but the final MOF crystal morphologies were irregular, with no visible rod structures (**Figure 1d-e**). PXRD patterns of these samples showed that the (100) peak was less intense in comparison with other crystallographic peaks. The preferred orientation of the samples was consistent with a lack of randomly oriented rods and a prominence of plate-like slabs that tended to orient parallel with the PXRD substrate,[4] and the overall intensity of the peaks was much less than in MOF samples synthesized with air, although peaks indicative of the intercalated layer were still present (See **Figure 1** & **Figure S9**). TEM analysis of the samples synthesized with H_2O_2 showed that the large particles observed in SEM are aggregates of smaller particles which show ordered crystalline domains (**Figures S10-13**). The yields of these reactions were also lower than the bubbled air condition (19% vs 39%, see **Table S3**). Additional SEM images as well as particle size analysis of all samples are shown in **Figures S14-19** and **Table S4**. XPS and EDX analysis showed that all samples contained carbon, oxygen, and nickel in similar ratios (see **Figures S20-27** and **Tables S5-6)**. Lowering the temperature of MOF formation reactions (from 85 °C to 40 °C or 22 °C, in the presence of bubbled air) produced slightly smaller rods and lowered overall yields, indicating the role of heat in driving $Ni_3(HHTP)_2$ self-assembly (see **Figures S28-29**, and **Table S7**). For MOFs, the nature of the link between synthesis temperature and MOF particle size varies depending on the specific MOF system.[77,78] However, the link we observed between lower reaction temperature and decreased $Ni_3(HHTP)_2$ nanorod size is consistent with trends observed in the hydrothermal synthesis of other crystalline nanomaterials, such as metal oxides.[79–82]

Mechanistic Insights into MOF Self-Assembly from *in situ* Spectroscopy. To gain deeper understanding of $Ni_3(HHTP)_2$ self-assembly, we investigated the rates of MOF deposition using *in situ* ATR-FTIR spectroscopy. Using a custom ATR reaction vessel (**Figure S30**), we examined

three characteristic bands (**Figure 2a**) corresponding to the vibrational modes of the MOF at 1464, 1314, and 1220 cm^{-1}, which were identified in previous reports of $Ni_3(HHTP)_2$.[42,56] An additional band at 1647 cm^{-1} corresponds to the bending mode of water;[83] the negative-going direction of this band indicates the likely displacement of water from the crystal upon the addition of MOF precursors to the reaction cell. The diagnostic MOF bands (which appear in the difference spectra of the initial solution subtracted from each reaction timepoint) correspond to absorbance bands observed in FTIR spectra of dried MOF powder regardless of particle morphology, and are not present in spectra of precursors HHTP and $Ni(OAc)_2$ (See **Figures S31-S32**). Although it is difficult to assign these bands to specific vibrational modes, past reports suggest that these energies correspond to vibrations within the aromatic ring system formed by HHTP coordinated with nickel ions.[42,84–86] The three bands grow in parallel over the course of MOF formation, although the band at 1464 cm^{-1} is always the largest, and without both nickel ions and HHTP present these bands do not appear (see **Figures S33-39**). The progress of MOF deposition onto the ATR crystal is represented by the increase in intensity of the band at 1464 cm^{-1} over the reaction time (**Figure 2b-c**).

Two important features characterize the reaction profiles in **Figure 2b-c**. Firstly, all reactions show an induction period, a region defined by minimal growth, immediately following the addition of oxidizing agent. This period is longest in the case when the cell is simply uncovered and exposed to air (3 hours) and shortest when H_2O_2 (16 equivalents, 50 µL 6% H_2O_2, 118 mM in cell) is added to the cell (12 minutes). When air is bubbled into the cell, the induction period is 40 minutes in length. The second feature is the initial region of growth following the induction period, a sharp increase in absorbance at 1464 cm^{-1} that was linear with respect to time. Initial rates were calculated based on this initial linear region of each growth trace (see **Figure S36**). The ‘air

bubbled' condition had a faster initial rate ($5.0 \pm 2.8 \times 10^{-4}$ min^{-1}) than the 'air diffusion' condition, which was an order of magnitude slower ($5.0 \pm 0.7 \times 10^{-5}$ min^{-1}). The addition of H_2O_2 approximately doubled the initial rate over that of the air bubbling condition ($9.6 \pm 6.8 \times 10^{-4}$ min^{-1}). Rates and induction periods for MOF growth experiments are summarized in **Table S8**.

To understand the correlation between growth rates and morphology, we collected MOF powders from syntheses mimicking the conditions used to collect rate data, analyzed them with SEM and PXRD, and calculated MOF yields. The yields of the collected MOF product were lower overall for these experiments, which occurred at room temperature, than that of the bulk synthesis reactions conducted at 85 °C (9.7 % vs 39 % for the 'air bubbled' condition, although yields were increased by running the reaction for longer than 18 hrs, see **Table S8**). SEM imaging showed that room temperature reaction conditions produced nanorods whether air is introduced through bubbling or diffusion. The rods appear shorter and more aggregated in the 'air bubbled' sample (**Figure 2d,f** and **Figures S40-41**) than in the 'air diffusion' sample (98 ± 38 nm vs. 275 ± 125 nm average length for air bubbled and air diffusion samples respectively, and similar differences in rod sizes were observed in samples collected after 6 days at room temperature, see **Figure S42**). By contrast, the H_2O_2 condition showed large (1.2 ± 0.9 μm), irregular particles (**Figure 2e, Figures S43-44**). PXRD analysis of these samples showed differences in relative crystallinity similar to samples from bulk synthesis experiments (**Figure S45**). The N_2 growth condition yielded less than 0.5 mg (<1% yield) of MOF and had no visible rod structures. Particle size analysis of all samples is shown in **Figures S46** and **Table S9**.

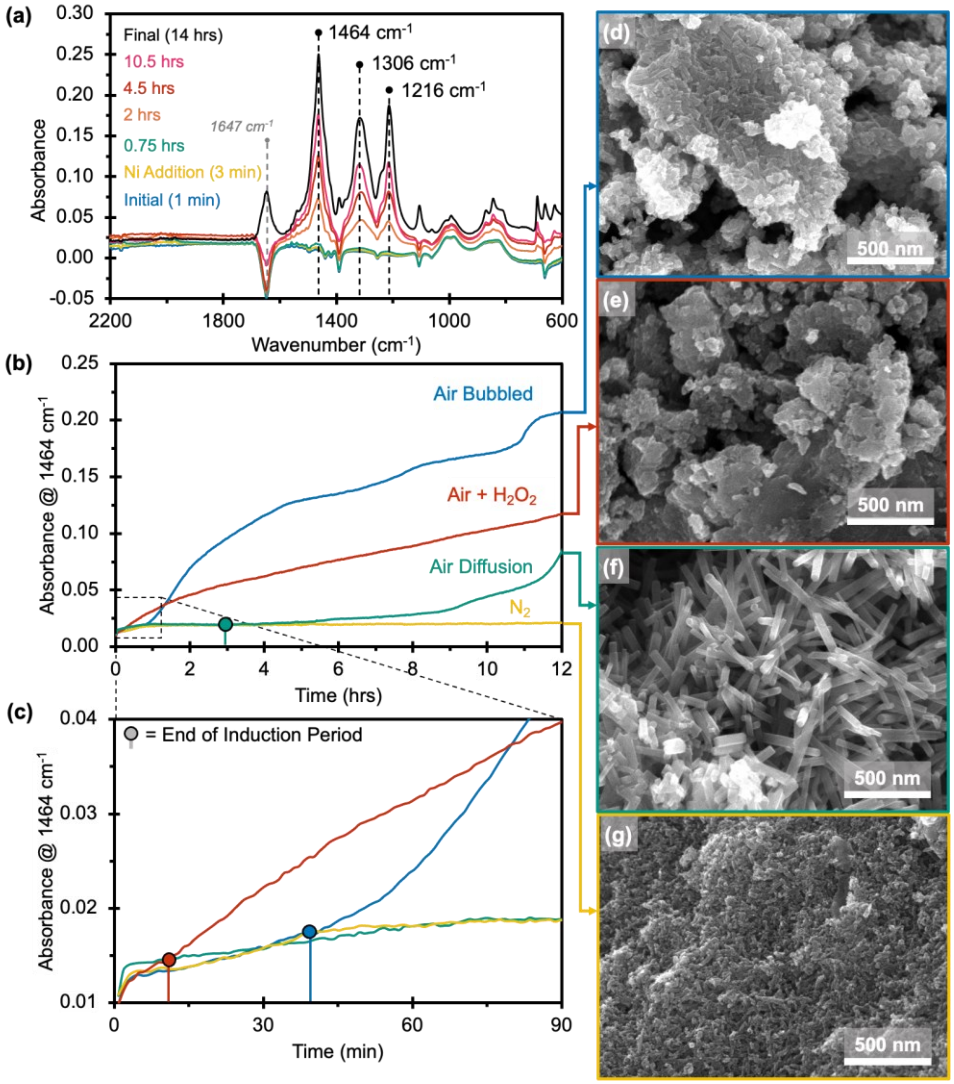

Figure 2. *In situ* ATR-FTIR monitoring of $Ni_3(HHTP)_2$ deposition. **(a)** FTIR absorbance spectra of the initial HHTP solution, the solution after the addition of nickel (II) acetate, and the difference spectra of the MOF deposited on the ATR crystal at reaction time points from 0.75 to 14 h of exposure to air (all spectra shown are difference spectra subtracting the initial solution baseline from the reaction timepoint). **(b)** Comparison of the deposition profiles at 1464 cm^{-1} for four reaction conditions: the cell open to air ('Air Diffusion') the cell with needle inserted bubbling air slowly through the solution ('Air Bubbled'), 50 µL 6% H_2O_2 added to the cell after the addition of the nickel solution and exposed to air ('Air + H_2O_2'), and the cell with N_2 gas flowing slowly over

reaction solution ('N_2'). **(c)** Expanded view of the first 90 minutes of MOF deposition. **(c-d)** The end of the induction period, which we defined as the point where MOF peaks became visible above the background, are marked on each trace with a circle. **(d-g)** SEM images of the morphology of $Ni_3(HHTP)_2$ samples collected from *in situ* IR experiments. All conditions shown used 11.1 mM HHTP dissolved in 20:3 water:DMF and a 2:1 Ni:HHTP ratio.

The variations in growth rates and morphologies correlated to reaction conditions further support the key role that oxidants play in the self-assembly of $Ni_3(HHTP)_2$. The oxidation of HHTP from the tris-catecholate to the tris-semiquinone state (accompanied by appropriate deprotonation) is necessary to achieve charge balance with the Ni^{2+} ions in the conjugated layer of the framework. Therefore, 3 equivalents of oxidant per 1 eq. HHTP in the conjugated layer are theoretically required for transformation from precursors into MOF. (The presence of the acetate counter ions assists in this transformation by aiding deprotonation of HHTP, which is also necessary for oxidation.) The reaction conditions described above reflect different regimes for oxidant concentration relative to HHTP. All reactions were set up with a deoxygenated solvent matrix. Exposure of the cell to air initiates the diffusion of oxygen into the reaction solution. The concentration of oxygen is therefore limited initially by the rate of O_2 diffusion at room temperature and ambient pressure. Additionally, the saturated concentration of oxygen in the solution at room temperature is expected to be an order of magnitude lower than that of HHTP (see **Table S10**), making O_2 the limiting reagent at the metal/linker concentrations used for all experiments (which reflect previously reported concentrations in the synthesis of this material).[4,27,42,54,55] Continued oxygen diffusion is necessary for MOF formation over the course of the reaction, and bubbling air into the reaction cell allows for faster diffusion of O_2 into the

solution, allowing the system to reach saturation more quickly than without bubbling air, and replenishing oxygen more quickly as it is consumed by the reaction. This hypothesis is supported by the fact that slowing oxygen diffusion by shrinking the aperture of the cell opening within the ATR-IR apparatus lengthens the induction period from 3 to 4.5 h, without a significant impact on the initial rate (see **Figure S47**).

By contrast, the 'Air + H_2O_2' condition is in a regime of higher oxidant concentration than reactions with air as the sole oxidant. In these reactions, the H_2O_2 concentration in the cell is in approximately a 15-fold excess relative to HHTP, leading to a shorter induction period of 8 ± 3 minutes. While nickel-containing materials have demonstrated catalytic activity towards the degradation of H_2O_2,[87,88] adding H_2O_2 to the nickel acetate solution produced no change in the UV absorbance over 18 hours, while the HHTP solution changed color from pale pink to brown following the addition of H_2O_2 over the same time period (**Figure S48**), indicating that the primary role of H_2O_2 in the MOF formation reaction is to oxidize the linker.

Correlation of Observed Growth Rates with Oxidant Concentrations. We next sought to correlate the initial rate of reaction with oxidant concentration by adding stoichiometric equivalents of oxidant to the reaction cell. The observed rate of $Ni_3(HHTP)_2$ growth increased with increasing concentrations of H_2O_2 from 0-10 molar equivalents. (**Figure 3a-b**). The initial rate (calculated based on the initial linear portion of the curve, approx. 10-30 min. depending on condition) for the 10 eq. H_2O_2 condition was approximately 10× greater than the observed rate for the 3 eq. and 1 eq. H_2O_2 conditions ($3.7 \pm 0.6 \times 10^{-3}$ min^{-1} vs. $4.1 \pm 2.2 \times 10^{-4}$ min^{-1}, and $2.8 \pm 1.3 \times 10^{-4}$, respectively, see **Table S11**). In most of these experiments, MOF growth proceeded immediately upon addition of oxidant with no observed induction period. However, when only 1 equivalent H_2O_2 was added to the reaction, an induction period of approximately 40 minutes was

observed (see **Figure S49**). PXRD analysis of samples from these reactions (isolated after allowing the reaction to proceed overnight) showed low intensity of diffraction peaks that were broad in nature (**Figure S50)**. SEM micrographs of these samples show a key feature: the 1 eq. and 3 eq. samples show some regions with irregularly shaped particles, but also regions containing small (<100 nm long) nanorods (**Figures 3d-e, S51,** see **Table S12** for additional particle size information). The presence of rod-like morphologies in these samples suggests that a slow initial growth rate is a critical factor in forming MOF nanorods.

This result was further supported by experiments in which H_2O_2 was added gradually to the reaction cell. Adding 2 equivalents H_2O_2 to the reaction cell at 0, 1, 2, 3, and 4 h (10 equivalents total, **Figure 3e**) resulted in a slower rate of deposition (average rate in the first hour of $1.7 \pm 0.3 \times 10^{-3}$ min^{-1} for the gradual addition versus $2.4 \pm 0.4 \times 10^{-3}$ min^{-1} when 10 equivalents was added at the start of the reaction). Similar average deposition rates were obtained when 2 eq. aliquots were added to the reaction at 30 minutes intervals (5 additions over 2 hours, $9.0 \pm 7.1 \times 10^{-4}$ min^{-1}, **Figure 3e**, **Table S13**). This reduction in deposition rate corresponded with a dramatic change in particle morphology and crystallinity. Rather than irregularly shaped particles, samples isolated from these reactions showed rod-shaped particles in SEM analysis (**Figure 3g,h**, **Figure S52, Table S14**), and PXRD patterns showed prominent (100) peaks (**Figure S53**) similar to the diffraction patterns of samples generated with air as the oxidant. These results indicate that the gradual infusion of H_2O_2 into the reaction cell moderates the rate of MOF deposition, allowing for the formation of material with larger crystalline domains. In this way, this gradual infusion of H_2O_2 mimicked the diffusion of oxygen from the air into the reaction solution and produced similar results.

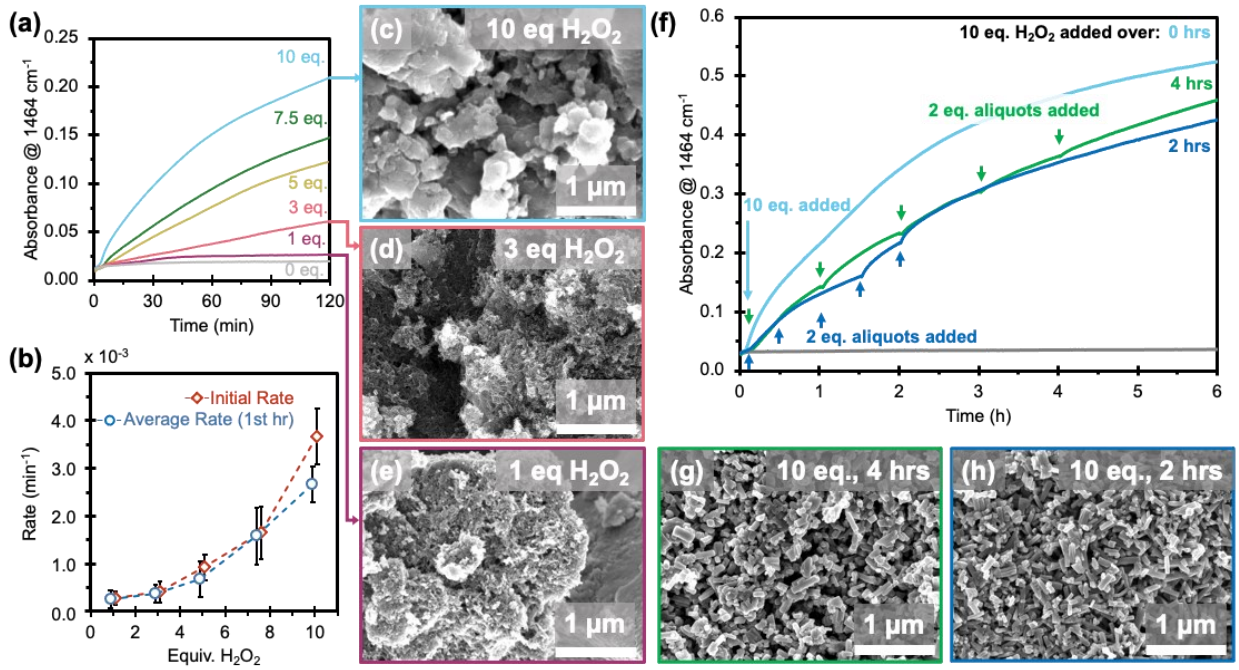

Figure 3. Impact of oxidant concentration on the morphology and self-assembly rates of $Ni_3(HHTP)_2$. **(a)** Deposition profiles of $Ni_3(HHTP)_2$ with 10, 7.5, 5, 3, 1, and 0 equivalents of H_2O_2 added at t = 3 min. All conditions shown used 11.1 mM HHTP dissolved in 20:3 water:DMF and a 2:1 Ni:HHTP ratio at room temperature. **(b)** Calculated rates of $Ni_3(HHTP)_2$ self-assembly for experiments with 1-10 eq. H_2O_2. Both initial rate (slope of the linear portion of the curve) and average rate (total change in the first 60 min of reaction) are shown. Error bars represent the standard deviation from the mean based on 3 replicates. **(c-e)** SEM images of samples isolated from **(c)** the 10-equivalent H_2O_2 condition, **(d)** the 3-equivalent H_2O_2 condition, and **(e)** the 1-equivalent H_2O_2 condition. **(f)** Deposition profiles of $Ni_3(HHTP)_2$ with 10 equivalents H_2O_2 added at t = 3 min, or introduced gradually in 5 aliquots over 2 or 4 hours. Colored arrows indicate the addition of aliquots to the cell. All conditions shown used 11.1 mM HHTP dissolved in 20:3 water:DMF and a 2:1 Ni:HHTP ratio at room temperature. **(g-h)** SEM images of samples isolated from **(g)** the 4-hour infusion condition and **(h)** the 2-hour infusion condition.

Less dramatic modulations in deposition rate can be observed when the flow rate of air bubbled into the reaction cell is varied using a mass flow controller. When air is flowed into the reaction at bubbling rates varying from 1 – 4 mL/min, the initial rate increases with increasing flow rate, and the length of the observed induction period decreases (**Figure 4a-b**). The difference in these rates is less extreme than the differences in rates between the 1 eq. and 10 eq. H_2O_2 conditions (a 2-fold increase between 1 and 4 mL/min experiments versus a 10-fold increase in the latter case, **Figure 4c-d, Table S15**). This result is consistent both with the relatively narrow range of flow rates explored due to experimental limitations (4 mL/min is the maximum flow rate of the mass flow controller) and with the fact that the maximum concentration of oxygen in the reaction is still limited by the maximum solubility of O_2 in the solvent matrix. Samples isolated from these reactions showed nanorod morphologies of similar sizes to particles generated from other experiments with air as the oxidant (**Figure 4e-g, Figure S54, Table S16**). These samples also showed prominent (100) peaks in PXRD patterns, consistent with rod-like morphologies (**Figure S55**).

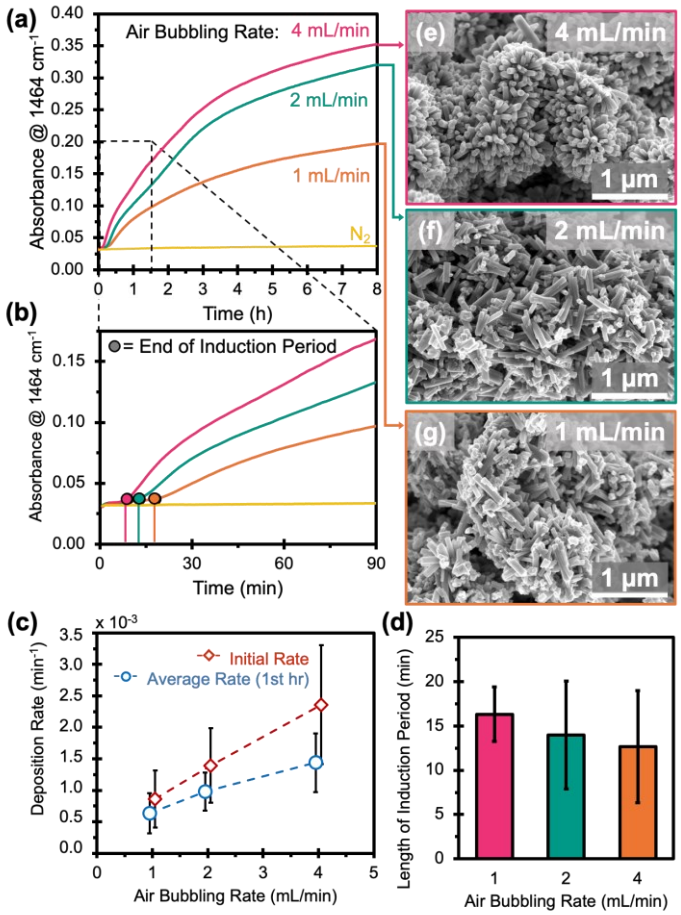

Figure 4. Impact of air bubbling rate on $Ni_3(HHTP)_2$ deposition rates and particle morphology. **(a)** Deposition profiles of $Ni_3(HHTP)_2$ with air bubbling into the reaction at 1, 2 and 4 mL/minute. All conditions shown used 11.1 mM HHTP dissolved in 20:3 water:DMF and a 2:1 Ni:HHTP ratio at room temperature. **(b)** Expanded view of the first 90 minutes of MOF deposition. **(c)** Calculated initial rates and average rates of $Ni_3(HHTP)_2$ deposition. **(d)** Observed length of induction periods for experiments with air bubbled into the reaction at a rate of 1, 2 and 4 mL/minute. **(e-g)** SEM images of samples isolated from **(e)** the1 mL/min condition, **(f)** the 2 mL/min condition, and **(e)** the 4 mL/min condition.

Observations of the Initial Phase of Self-Assembly of MOF. While the induction period observed in ATR-FTIR experiments results in no deposition of MOF on the ATR crystal, important processes are occurring during this time. One such process is the solution-phase formation of Ni-HHTP coordination complexes, which can then self-assemble into larger, solid-phase MOF crystals. The formation of such a complex is supported by UV-vis spectroscopy, which showed an immediate color change and new maximum absorbance of approximately 600 nm upon the addition of $Ni(OAc)_2$ to the HHTP solution (**Figure 5a**). This observed peak is similar in position to those of previously reported nickel-catecholate complexes,[85] and increased in intensity over the period of an hour, with or without oxidant, corresponding to a darkening of the navy-blue color of the solution (**Figures 5b, S56**). A detailed study of analogous ruthenium-HHTP complexes by Ward and colleagues suggests that this new peak in the red region of the visible spectrum is a combination of ligand-centered $\pi \rightarrow \pi^*$ transitions and metal-to-ligand charge transfer, and that the red shifting of the peak over time is consistent with oxidation of the Ni-HHTP complexes.[76] In addition to the growth of the peak at 604 nm, the absorbance from 750-800 nm increased, and the cuvette also became visibly less translucent over this period, consistent with increases in turbidity observed in the crystallization of other framework materials.[51,89] This initial nucleation can also be observed in FTIR studies as a small initial rise in absorbance at 1464 cm^{-1} (**Figure 5c**). Excluding oxidant from the reaction system halts reaction progress, with no observable MOF precipitation. Delaying oxidant addition by two hours effectively leads to reaction arrest, as evidenced by the absorbance at 1464 cm^{-1}, which remains approximately constant in that time. Taken together, these changes suggest that in the absence of oxidant, formation of Ni-HHTP complexes and oligomers in solution is possible, but significant growth of MOF nanocrystals only begins after the oxidant (H_2O_2) is added to the reaction (**Figure 5d**).

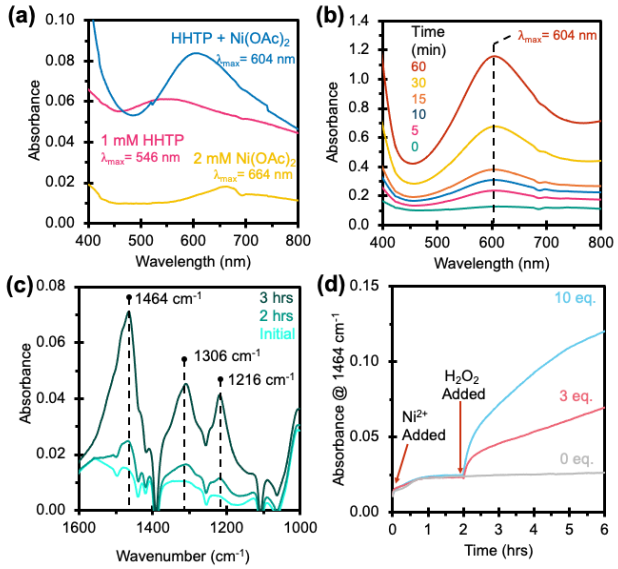

Figure 5. The role of the Ni^{2+}-HHTP coordination complex in $Ni_3(HHTP)_2$ MOF formation. **(a)** Visible absorption spectrum of HHTP solution, $Ni(OAc)_2$ solution, and Ni and HHTP solutions combined. **(b)** The visible spectrum of the first hour following addition of $Ni(OAc)_2$ solution to HHTP solution in a sealed cuvette (double beam with DMF/H_2O solution matrix blank). **(c)** FTIR difference spectra of reaction mixture immediately after addition on Ni^{2+} (initial), at 2 hours (prior to addition of oxidant) and 3 hours (1 hour post-addition of 10 eq. H_2O_2) **(d)** Deposition profile for experiments with delayed addition of 3 and 10 equivalents H_2O_2, added two hours after combination of $Ni(OAc)_2$ and HHTP solutions.

Comparing the initial rates of reaction in the experiments with delayed and immediate addition of H_2O_2 further supports the vital role of the Ni-HHTP coordination complex in MOF self-assembly and the impact of oxidants on MOF morphology. The initial rate for the 10 eq. condition is not significantly changed with delayed H_2O_2 addition, but the rate for the 3 eq. condition is approximately 3× greater when H_2O_2 is added after 2 hours ($4.1 \pm 2.2 \times 10^{-4}$ vs. $1.3 \pm 0.7 \times 10^{-3}$ min^{-1}, respectively, see **Table S11**). This result indicates that after Ni-HHTP subunits have

assembled, the addition of oxidant allows MOF growth to proceed rapidly. This 'pre-assembly' of the Ni-HHTP coordination complex prior to the introduction of oxidant dramatically impacts the resulting morphology of the MOF. The morphologies of the MOF samples collected from these reactions (allowed to continue over 18 hours before isolation) are similar to other MOF samples with large excesses of H_2O_2, with SEM images showing large, irregularly shaped particles, indicating that rapid precipitation is the cause of these aggregated MOF particles (See **Figures S57-S58**) for additional SEM images and PXRD characterization). These results demonstrate how the manipulation of growth rates and induction periods for $Ni_3(HHTP)_2$ directly impacts the morphology of the synthesized MOF particles.

The observed phases of MOF growth in this study, comprising an induction period, followed by linear growth, followed by a plateau, are similar to those observed in the growth of COF-5, an HHTP- based COF.[51,89] In the case of COF-5, the initial rate and length of the induction period are highly dependent on the temperature and concentrations of framework components. Temperature governs the length of COF-formation processes because the energy barrier for the reaction between HHTP and the 1,4-phenylene bis(boronic acid) linker is relatively high, compared with the rapid, low activation energy process of stacking once extended layers form, such that the observed rate of COF growth is a combination of the parallel processes of oligomer formation and layer stacking.[51] Although the structure of COF-5 is not totally analogous to that of $Ni_3(HHTP)_2$, the stacking of the layers of both materials consists of $\pi - \pi$ interactions of triphenylene subunits.[27,84] Computational analysis of COF-5 self-assembly suggests that stacking between larger layers is more stable than stacking of smaller layers, leading to the formation of insoluble COF nuclei.[51] These mechanistic insights into COF formation are useful in interpreting the kinetic results presented here, and in theorizing potential mechanisms for HHTP-based MOF nucleation and

growth. Similar to COF-5, the overall growth rate of $Ni_3(HHTP)_2$ is a combination of at least two processes: 1) coordination-polymerization of ligand monomers and Ni^{2+} ions into the conjugated layer, and 2) the stacking of layers to form the layered MOF crystals. We have determined that the initial coordination of Ni^{2+} ions with ligand proceeds rapidly, but the nucleation of MOF crystallites (corresponding to the observed induction period) is governed by the presence of oxidants. This result indicates that oxidation is a necessary step of the coordination–polymerization of the ligand and Ni^{2+}. To form the metal (bis-dioxolene) linkages that extend into a charge-neutral coordination polymer, the ligand must be appropriately oxidized and charge-balanced to provide a charge-neutral extended framework compensating the 2+ charge of Ni-ions[90] (see **Figure S59** for the structure of the monomer units and intercalated layer). As layers grow larger, they can begin to stack, and result in solid crystals (see **Figure 6**).

In all cases, oxidants are critical to the formation of $Ni_3(HHTP)_2$ crystallites. In a typical, hydrothermal, heterogeneous synthesis of $Ni_3(HHTP)_2$ under ambient atmosphere, the starting HHTP/nickel acetate/water mixture is not degassed and thus contains dissolved oxygen. In such reactions, HHTP is typically present at mM concentrations, meaning that, as in the experiments presented above, oxygen is the limiting reagent, and must be replenished through the course of the reaction. Thus, the diffusion of oxygen governs the rate at which the MOF can self-assemble, and as we have shown here, adding large excesses of oxidant at the beginning of the reaction can speed up the precipitation of MOF solid, but results in large, irregularly shaped particles. In order to fabricate $Ni_3(HHTP)_2$ MOF particles with consistent size and morphology,[4] control of growth kinetics is essential, and a critical factor in controlling growth kinetics is the concentration of oxidants.

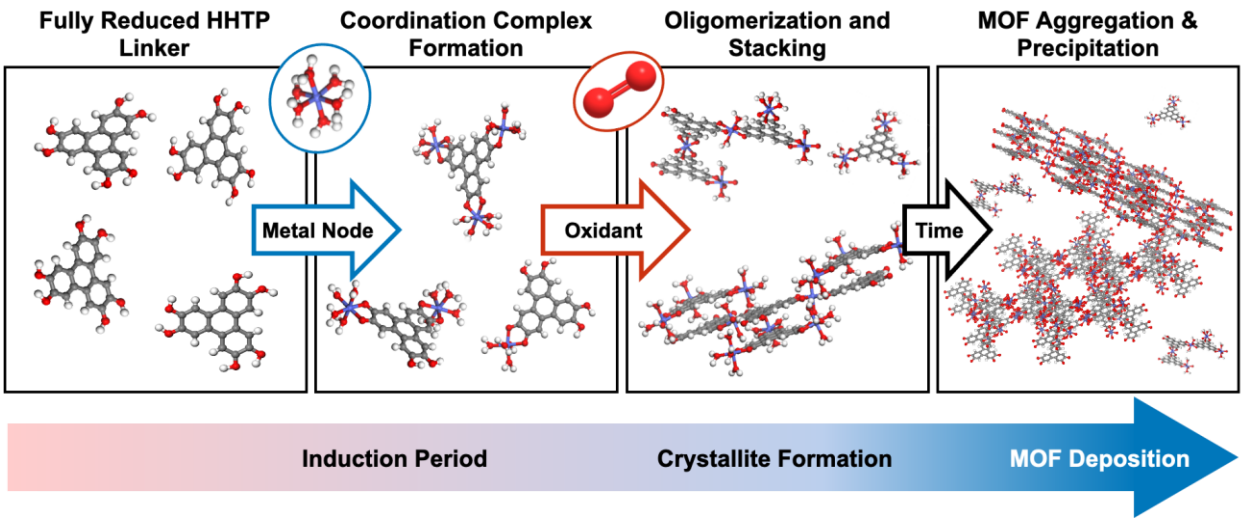

Figure 6. Schematic diagram depicting the proposed mechanistic domains of $Ni_3(HHTP)_2$ formation. The formation of Ni(catecholate) coordination complexes proceeds immediately after the addition of $Ni(OAc)_2$. Without oxygen, the complexes cannot form Ni bis(dioxolene) structures, which precludes the formation of higher oligomers and eventually MOF crystallites. Addition of an oxidant at this step oxidizes the HHTP coordination complex, which leads to a brief induction period where the 2D coordination-polymerization and stacking processes begin, followed by MOF aggregation and precipitation.

CONCLUSION

This paper presents a novel approach to monitoring the growth and deposition of $Ni_3(HHTP)_2$ MOF particles, which is used as a model system for understanding the self-assembly process of layered, conductive MOF nanocrystals. Our *in situ* observations demonstrated three key aspects of $Ni_3(HHTP)_2$ self-assembly and deposition: Firstly, the presence and identity of oxidants is crucial to the precipitation of solid MOF from reaction components and impact the morphology of the resulting MOF particles. Secondly, observable MOF growth proceeds after an induction period,

during which Ni-HHTP coordination complexes form in solution. Finally, the observed rates of MOF growth are driven by the concentrations of oxidants added to the system.

Based on these observations, we propose a possible mechanism for the nucleation of HHTP MOFs from precursor components, in which reduced HHTP coordinates with nickel ions in solution. The combination of these coordination complexes and oxidizing agents allows for the formation of extended layers of HHTP ligands coordinated to nickel ions and drives the formation of oligomers, which combine and stack to form crystalline MOF particles. Although initial coordination between Ni^{2+} and HHTP may proceed without an oxidant, the process likely does not lead to the formation of extended MOF layers, instead terminating at the point of coordination complex formation. This initial coordination step is a necessary, but insufficient step for self-assembly into MOF crystallites. Without oxidant, the reaction is stalled at this step, making the coordination-polymerization process inaccessible. Speeding up oxidation, for example, by adding H_2O_2 to the reaction, increases the rate of this process, but faster growth leads to irregularly shaped particles, suggesting that a slow, self-correcting process — the rate of which can be controlled by the identity and concentration of the oxidant — is necessary for the formation of nanocrystalline MOF particles.

Our *in situ* studies provide valuable insights into the role of oxidants in $Ni_3(HHTP)_2$ self-assembly, but a key limitation is the lack of control over temperature in the ATR-FTIR reaction cell used in this study. Our studies demonstrate that $Ni_3(HHTP)_2$ self-assembly can occur at room temperature, but the impact of heat and pH on the rates of MOF formation and the resulting particle morphology are still unexplored. This limitation could be overcome with a more sophisticated design of a reaction cell, which would also allow for the study of other MOF systems that do not form at room temperature. Another limitation is inherent to the use of attenuated total reflectance,

namely that it only captures the deposition of MOF particles on a surface and cannot provide insight into the nucleation of particles in solution. Finally, we were unable to isolate fully reduced HHTP-tc which limited our ability to precisely measure how HHTP-tc behaves in its coordination process with Ni^{2+}.

Nevertheless, this work gives new context to previously reported methods for the synthesis of HHTP-based MOFs, particularly interfacial and surface deposition methods.[4,54,56,61–63] Our results show that the diffusion of oxidizing agents plays a key role in the kinetics of MOF formation, suggesting that particular MOF morphologies, such as oriented thin films, can be generated with careful control of the concentration and identity of the oxidant. Strategic design of reaction vessel geometries and consideration of other synthetic parameters allows for the controlled diffusion of oxygen into the system, leading to slow, and often highly oriented MOF growth.[4,56] We anticipate that the same principles and methods can be applied to the study of the growth of other layered conductive MOFs. On a fundamental level, understanding of the experimental conditions that impact growth and deposition for other $M_3(HXTP)_2$ materials will lead to new understanding of the layered packing structure of triphenylene-based MOFs, particularly those that form without an intercalated layer. More practically, the insights we present here are poised to allow for the development of new methods for depositing layered conductive MOF onto surfaces and incorporating these materials into functional devices such as portable chemical sensors,[1] electrocatalysts,[11] energy storage devices,[6] and magnetoelectronic systems.[22]

EXPERIMENTAL METHODS

A complete account of methods, supporting characterization, and experimental results can be found in the **Supporting Information.**

Bulk synthesis of $Ni_3(HHTP)_2$. The synthesis of $Ni_3(HHTP)_2$ was modified from previously reported methods[27,54,62] to form MOF from a homogeneous solution. Into a 1 dram (20 mL) vial with a septa top was added 10 mL of a solvent mixture consisting of 20 parts DI H_2O and 3 parts DMF. The flask was sparged with N_2 for 10 min. Once free of oxygen, HHTP (36 mg, 0.111 mmol) was added to the vial and sonicated until fully dissolved. In a separate vial was dissolved $Ni(OAc)_2(H_2O)_4$ (55 mg, 0.222 mmol) in the same degassed H_2O/DMF solvent system. Once dissolved and degassed, the solution of $Ni(OAc)_2$ was added via syringe to the vial containing the solution of HHTP. The reaction was kept under the desired atmosphere (air or N_2 bubbled through the solution) at the desired temperature (25 °C or 85 °C) for 18 hours. The reaction contents were then collected via vacuum filtration and rinsed 5 times each with 10 mL of acetone followed by 10 mL of water. The resulting blue-black powder was dried and stored under vacuum.

In-situ monitoring of $Ni_3(HHTP)_2$ growth by ATR-FTIR: Details of FTIR instrumentation, and the construction of a custom ATR-FTIR reaction cell are detailed in **Section IV** of the **Supporting Information**. Reactions performed on the ATR-FTIR were run for 14 hours. To monitor the reaction, we collected spectra from 400–4000 cm^{-1} every 60 seconds. The spectra were collected as double beam experiments subtracted from a single beam taken of the starting HHTP solution. In a typical experiment, 36 mg HHTP was dissolved in 10 mL solvent mixture [degassed water:DMF (20:3 vol:vol)] in a septa-topped vial purged with nitrogen, and 55.3 mg $Ni(OAc)_2 \bullet 4H_2O$ was dissolved in 5 mL of solvent mixture in a septa-topped vial purged with nitrogen. 500 µL HHTP solution was added via syringe to the reaction cell, and background spectra were collected, with nitrogen flowing over the cell headspace. 250 µL Ni solution was added to the reaction cell, the desired oxidant was introduced (air bubbled through solution, nitrogen flow removed and cell left open to air, or H_2O_2 added) and spectra were collected every 60 s for 14

hours. All spectra shown are difference spectra, reflecting changes in absorbance from the initial HHTP solution. The remaining nickel acetate solution was added to the remaining HHTP solution, and the desired oxidant was introduced. The reaction was left at room temperature for 18 hours, after which time the MOF was collected via vacuum filtration and washed with water and ethanol, so that MOF samples could be collected for PXRD and SEM analysis.

ASSOCIATED CONTENT

Supporting Information.

The following files are available free of charge.

Additional experimental details, synthetic details, scanning electron micrographs, powder x-ray diffraction (PXRD) and X-ray photoelectron spectroscopy (XPS) for MOF samples, as well as additional *in situ* MOF growth spectra and reaction profiles (PDF)

AUTHOR INFORMATION

Corresponding Author

*Katherine A. Mirica – Department of Chemistry, Burke Laboratory, Dartmouth College, Hanover, New Hampshire 03755, United States

Email: Katherine.a.mirica@dartmouth.edu

Other Authors

Emma K. Ambrogi – Department of Chemistry, Burke Laboratory, Dartmouth College, Hanover, New Hampshire 03755, United States ORCID: **https://orcid.org/0009-0002-7615-501X**

Patrick Damacet – Department of Chemistry, Burke Laboratory, Dartmouth College, Hanover, New Hampshire 03755, United States ORCID: https://orcid.org/0000-0002-8039-1405

Robert M. Stolz† – Department of Chemistry, Burke Laboratory, Dartmouth College, Hanover, New Hampshire 03755, United States ORCID: https://orcid.org/0000-0002-9291-0794

Present Addresses

†Robert Manuel Stolz, Department of Chemistry, Lokey Laboratory Building, 337 Campus Drive, Stanford University, Stanford California, 94305. ORCID: https://orcid.org/0000-0002-9291-0794

Author Contributions

Experimental work was performed by E.K.A and P.D. Analysis of experimental results was performed by E.K.A, P.D, and K.A.M. The project was defined and guided by K.A.M. The manuscript was written by E.K.A and K.A.M with contributions from all authors. The project was conceived by R.M.S with contributions from all authors. All authors have given approval to the final version of the manuscript.

Notes

The authors declare no competing financial interest.

ACKNOWLEDGMENTS

The authors acknowledge funding support from the National Institutes of Health (NIH) MIRA award (#R35GM138318), NSF CAREER Award (#1945218), and the Dreyfus Teacher-Scholar Award. The authors would like to thank John Wilderman of the University of New Hampshire Instrumentation Center for assistance in collecting XPS measurements.

REFERENCES

(1) Meng, Z.; Stolz, R. M.; Mendecki, L.; Mirica, K. A. Electrically-Transduced Chemical Sensors Based on Two-Dimensional Nanomaterials. *Chem. Rev.* **2019**, *119*, 478–598.

(2) Nath, A.; Asha, K. S.; Mandal, S. Conductive Metal-Organic Frameworks: Electronic Structure and Electrochemical Applications. *Chem. – Eur. J.* **2021**, *27*, 11482–11538.
(3) Zhang, L.; Zhou, Y.; Han, S. The Role of Metal–Organic Frameworks in Electronic Sensors. *Angew. Chem. Int. Ed.* **2021**, *60*, 15192–15212.
(4) Stolz, R. M.; Kolln, A. F.; Rocha, B. C.; Brinks, A.; Eagleton, A. M.; Mendecki, L.; Vashisth, H.; Mirica, K. A. Epitaxial Self-Assembly of Interfaces of 2D Metal–Organic Frameworks for Electroanalytical Detection of Neurotransmitters. *ACS Nano* **2022**, *16*, 13869–13883.
(5) Luo, Y.; Wu, Y.; Braun, A.; Huang, C.; Li, X.; Menon, C.; Chu, P. K. Defect Engineering To Tailor Metal Vacancies in 2D Conductive Metal–Organic Frameworks: An Example in Electrochemical Sensing. *ACS Nano* **2022**, *16*, 20820–20830.
(6) Guo, Y.; Wang, K.; Hong, Y.; Wu, H.; Zhang, Q. Recent Progress on Pristine Two-Dimensional Metal–Organic Frameworks as Active Components in Supercapacitors. *Dalton Trans.* **2021**, *50*, 11331–11346.
(7) Wang, M.; Dong, R.; Feng, X. Two-Dimensional Conjugated Metal–Organic Frameworks (2D *c* -MOFs): Chemistry and Function for MOFtronics. *Chem. Soc. Rev.* **2021**, *50*, 2764–2793.
(8) Lukatskaya, M. R.; Feng, D.; Bak, S.-M.; To, J. W. F.; Yang, X.-Q.; Cui, Y.; Feldblyum, J. I.; Bao, Z. Understanding the Mechanism of High Capacitance in Nickel Hexaaminobenzene-Based Conductive Metal–Organic Frameworks in Aqueous Electrolytes. *ACS Nano* **2020**, *14*, 15919–15925.
(9) Zhang, P.; Yang, S.; Xie, H.; Li, Y.; Wang, F.; Gao, M.; Guo, K.; Wang, R.; Lu, X. Advanced Three-Dimensional Microelectrode Architecture Design for High-Performance On-Chip Micro-Supercapacitors. *ACS Nano* **2022**, *16*, 17593–17612.
(10) Hendon, C. H.; Rieth, A. J.; Korzyński, M. D.; Dincă, M. Grand Challenges and Future Opportunities for Metal–Organic Frameworks. *ACS Cent. Sci.* **2017**, *3*, 554–563.
(11) Dhakshinamoorthy, A.; Asiri, A. M.; Garcia, H. 2D Metal–Organic Frameworks as Multifunctional Materials in Heterogeneous Catalysis and Electro/Photocatalysis. *Adv. Mater.* **2019**, *31*, 1900617.
(12) Banerjee, S.; Anayah, R. I.; Gerke, C. S.; Thoi, V. S. From Molecules to Porous Materials: Integrating Discrete Electrocatalytic Active Sites into Extended Frameworks. *ACS Cent. Sci.* **2020**, *6*, 1671–1684.
(13) Liu, W.; Ni, C.; Gao, M.; Zhao, X.; Zhang, W.; Li, R.; Zhou, K. Metal–Organic-Framework-Based Nanoarrays for Oxygen Evolution Electrocatalysis. *ACS Nano* **2023**, *17*, 24564–24592.
(14) Zhong, H.; Wang, M.; Chen, G.; Dong, R.; Feng, X. Two-Dimensional Conjugated Metal–Organic Frameworks for Electrocatalysis: Opportunities and Challenges. *ACS Nano* **2022**, *16*, 1759–1780.
(15) Sun, L.; Campbell, M. G.; Dincă, M. Electrically Conductive Porous Metal-Organic Frameworks. *Angew. Chem. Int. Ed.* **2016**, *55*, 3566–3579.
(16) Xie, L. S.; Skorupskii, G.; Dincă, M. Electrically Conductive Metal–Organic Frameworks. *Chem. Rev.* **2020**, *120*, 8536–8580.
(17) Park, C.; Baek, J. W.; Shin, E.; Kim, I.-D. Two-Dimensional Electrically Conductive Metal–Organic Frameworks as Chemiresistive Sensors. *ACS Nanosci. Au* **2023**, *3*, 353–374.
(18) Ko, M.; Mendecki, L.; Mirica, K. A. Conductive Two-Dimensional Metal–Organic Frameworks as Multifunctional Materials. *Chem. Commun.* **2018**, *54*, 7873–7891.

(19) Ma, X.; Kang, J.; Wu, Y.; Pang, C.; Li, S.; Li, J.; Xiong, Y.; Luo, J.; Wang, M.; Xu, Z. Recent Advances in Metal/Covalent Organic Framework-Based Materials for Photoelectrochemical Sensing Applications. *TrAC Trends Anal. Chem.* **2022**, *157*, 116793.
(20) Zhang, X.; Tian, X.-L.; Qin, Y.; Qiao, J.; Pan, F.; Wu, N.; Wang, C.; Zhao, S.; Liu, W.; Cui, J.; Qian, Z.; Zhao, M.; Liu, J.; Zeng, Z. Conductive Metal–Organic Frameworks with Tunable Dielectric Properties for Boosting Electromagnetic Wave Absorption. *ACS Nano* **2023**, *17*, 12510–12518.
(21) Mähringer, A.; Jakowetz, A. C.; Rotter, J. M.; Bohn, B. J.; Stolarczyk, J. K.; Feldmann, J.; Bein, T.; Medina, D. D. Oriented Thin Films of Electroactive Triphenylene Catecholate-Based Two-Dimensional Metal–Organic Frameworks. *ACS Nano* **2019**, *13*, 6711–6719.
(22) Yan, X.; Su, X.; Chen, J.; Jin, C.; Chen, L. Two-Dimensional Metal-Organic Frameworks Towards Spintronics. *Angew. Chem. Int. Ed.* **2023**, *62*, e202305408.
(23) Wang, Y.; Qian, Y.; Zhang, L.; Zhang, Z.; Chen, S.; Liu, J.; He, X.; Tian, Y. Conductive Metal–Organic Framework Microelectrodes Regulated by Conjugated Molecular Wires for Monitoring of Dopamine in the Mouse Brain. *J. Am. Chem. Soc.* **2023**, *145*, 2118–2126.
(24) Wang, J.; Liu, S.; Luo, J.; Hou, S.; Song, H.; Niu, Y.; Zhang, C. Conductive Metal-Organic Frameworks for Amperometric Sensing of Paracetamol. *Front. Chem.* **2020**, *8*, 594093.
(25) Wang, B.; Luo, Y.; Gao, L.; Liu, B.; Duan, G. High-Performance Field-Effect Transistor Glucose Biosensors Based on Bimetallic Ni/Cu Metal-Organic Frameworks. *Biosens. Bioelectron.* **2021**, *171*, 112736.
(26) Xu, Z.; Wang, Q.; Zhangsun, H.; Zhao, S.; Zhao, Y.; Wang, L. Carbon Cloth-Supported Nanorod-like Conductive Ni/Co Bimetal MOF: A Stable and High-Performance Enzyme-Free Electrochemical Sensor for Determination of Glucose in Serum and Beverage. *Food Chem.* **2021**, *349*, 129202.
(27) Hmadeh, M.; Lu, Z.; Liu, Z.; Gándara, F.; Furukawa, H.; Wan, S.; Augustyn, V.; Chang, R.; Liao, L.; Zhou, F.; Perre, E.; Ozolins, V.; Suenaga, K.; Duan, X.; Dunn, B.; Yamamto, Y.; Terasaki, O.; Yaghi, O. M. New Porous Crystals of Extended Metal-Catecholates. *Chem. Mater.* **2012**, *24*, 3511–3513.
(28) Skorupskii, G.; Trump, B. A.; Kasel, T. W.; Brown, C. M.; Hendon, C. H.; Dincă, M. Efficient and Tunable One-Dimensional Charge Transport in Layered Lanthanide Metal–Organic Frameworks. *Nat. Chem.* **2020**, *12*, 131–136.
(29) Choi, J. Y.; Stodolka, M.; Kim, N.; Pham, H. T. B.; Check, B.; Park, J. 2D Conjugated Metal-Organic Framework as a Proton-Electron Dual Conductor. *Chem* **2023**, *9*, 143–153.
(30) Dou, J.-H.; Sun, L.; Ge, Y.; Li, W.; Hendon, C. H.; Li, J.; Gul, S.; Yano, J.; Stach, E. A.; Dincă, M. Signature of Metallic Behavior in the Metal–Organic Frameworks M_3(Hexaiminobenzene)$_2$ (M = Ni, Cu). *J. Am. Chem. Soc.* **2017**, *139*, 13608–13611.
(31) Park, J.; Hinckley, A. C.; Huang, Z.; Feng, D.; Yakovenko, A. A.; Lee, M.; Chen, S.; Zou, X.; Bao, Z. Synthetic Routes for a 2D Semiconductive Copper Hexahydroxybenzene Metal–Organic Framework. *J. Am. Chem. Soc.* **2018**, *140*, 14533–14537.
(32) Campbell, M. G.; Sheberla, D.; Liu, S. F.; Swager, T. M.; Dincă, M. Cu_3(Hexaiminotriphenylene$_2$: An Electrically Conductive 2D Metal-Organic Framework for Chemiresistive Sensing. *Angew. Chem. Int. Ed.* **2015**, *54*, 4349–4352.
(33) Meng, Z.; Mirica, K. A. Two-Dimensional d-π Conjugated Metal-Organic Framework Based on Hexahydroxytrinaphthylene. *Nano Res.* **2021**, *14*, 369–375.
(34) Lu, Y.; Hu, Z.; Petkov, P.; Fu, S.; Qi, H.; Huang, C.; Liu, Y.; Huang, X.; Wang, M.; Zhang, P.; Kaiser, U.; Bonn, M.; Wang, H. I.; Samorì, P.; Coronado, E.; Dong, R.; Feng, X. Tunable

Charge Transport and Spin Dynamics in Two-Dimensional Conjugated Metal–Organic Frameworks. *J. Am. Chem. Soc.* **2024**, *146*, 2574–2582.
(35) Lu, Y.; Zhang, Y.; Yang, C.-Y.; Revuelta, S.; Qi, H.; Huang, C.; Jin, W.; Li, Z.; Vega-Mayoral, V.; Liu, Y.; Huang, X.; Pohl, D.; Položij, M.; Zhou, S.; Cánovas, E.; Heine, T.; Fabiano, S.; Feng, X.; Dong, R. Precise Tuning of Interlayer Electronic Coupling in Layered Conductive Metal-Organic Frameworks. *Nat. Commun.* **2022**, *13*, 7240.
(36) Borysiewicz, M. A.; Dou, J.-H.; Stassen, I.; Dincă, M. Why Conductivity Is Not Always King – Physical Properties Governing the Capacitance of 2D Metal–Organic Framework-Based EDLC Supercapacitor Electrodes: A $Ni_3(HITP)_2$ Case Study. *Faraday Discuss.* **2021**, *231*, 298–304.
(37) Lee, T.; Kim, J.; Park, C.; Kim, H.; Kim, M.; Park, H.; Kim, I.; Ko, J.; Pak, K.; Choi, S. Q.; Kim, I.; Park, S. Large-Area Synthesis of Ultrathin, Flexible, and Transparent Conductive Metal–Organic Framework Thin Films via a Microfluidic-Based Solution Shearing Process. *Adv. Mater.* **2022**, *34*, 2107696.
(38) Wong, Y. T. A.; Martins, V.; Lucier, B. E. G.; Huang, Y. Solid-State NMR Spectroscopy: A Powerful Technique to Directly Study Small Gas Molecules Adsorbed in Metal–Organic Frameworks. *Chem. – Eur. J.* **2019**, *25*, 1848–1853.
(39) Nandy, A.; Forse, A. C.; Witherspoon, V. J.; Reimer, J. A. NMR Spectroscopy Reveals Adsorbate Binding Sites in the Metal–Organic Framework UiO-66(Zr). *J. Phys. Chem. C* **2018**, *122*, 8295–8305.
(40) Sha, F.; Tai, T.-Y.; Gaidimas, M. A.; Son, F. A.; Farha, O. K. Leveraging Isothermal Titration Calorimetry to Obtain Thermodynamic Insights into the Binding Behavior and Formation of Metal–Organic Frameworks. *Langmuir* **2022**, *38*, 6771–6779.
(41) Kato, S.; Drout, R. J.; Farha, O. K. Isothermal Titration Calorimetry to Investigate Uremic Toxins Adsorbing onto Metal-Organic Frameworks. *Cell Rep. Phys. Sci.* **2020**, *1*, 100006.
(42) Stolz, R. M.; Mahdavi-Shakib, A.; Frederick, B. G.; Mirica, K. A. Host–Guest Interactions and Redox Activity in Layered Conductive Metal–Organic Frameworks. *Chem. Mater.* **2020**, *32*, 7639–7652.
(43) Miner, E. M.; Wang, L.; Dincă, M. Modular O_2 Electroreduction Activity in Triphenylene-Based Metal–Organic Frameworks. *Chem. Sci.* **2018**, *9*, 6286–6291.
(44) Day, R. W.; Bediako, D. K.; Rezaee, M.; Parent, L. R.; Skorupskii, G.; Arguilla, M. Q.; Hendon, C. H.; Stassen, I.; Gianneschi, N. C.; Kim, P.; Dincă, M. Single Crystals of Electrically Conductive Two-Dimensional Metal–Organic Frameworks: Structural and Electrical Transport Properties. *ACS Cent. Sci.* **2019**, *5*, 1959–1964.
(45) Nam, K. W.; Park, S. S.; Dos Reis, R.; Dravid, V. P.; Kim, H.; Mirkin, C. A.; Stoddart, J. F. Conductive 2D Metal-Organic Framework for High-Performance Cathodes in Aqueous Rechargeable Zinc Batteries. *Nat. Commun.* **2019**, *10*, 4948.
(46) Eagleton, A. M.; Ko, M.; Stolz, R. M.; Vereshchuk, N.; Meng, Z.; Mendecki, L.; Levenson, A. M.; Huang, C.; MacVeagh, K. C.; Mahdavi-Shakib, A.; Mahle, J. J.; Peterson, G. W.; Frederick, B. G.; Mirica, K. A. Fabrication of Multifunctional Electronic Textiles Using Oxidative Restructuring of Copper into a Cu-Based Metal–Organic Framework. *J. Am. Chem. Soc.* **2022**, *144*, 23297–23312.
(47) Aykanat, A.; Jones, C. G.; Cline, E.; Stolz, R. M.; Meng, Z.; Nelson, H. M.; Mirica, K. A. Conductive Stimuli-Responsive Coordination Network Linked with Bismuth for Chemiresistive Gas Sensing. *ACS Appl. Mater. Interfaces* **2021**, *13*, 60306–60318.

(48) Gao, Z.; Hou, M.; Shi, Y.; Li, L.; Sun, Q.; Yang, S.; Jiang, Z.; Yang, W.; Zhang, Z.; Hu, W. A Conductive Catecholate-Based Framework Coordinated with Unsaturated Bismuth Boosts CO_2 Electroreduction to Formate. *Chem. Sci.* **2023**, *14*, 6860–6866.
(49) Snook, K. M.; Zasada, L. B.; Chehada, D.; Xiao, D. J. Oxidative Control over the Morphology of $Cu_3(HHTP)_2$, a 2D Conductive Metal–Organic Framework. *Chem. Sci.* **2022**, *13*, 10472–10478.
(50) Evans, A. M.; Parent, L. R.; Flanders, N. C.; Bisbey, R. P.; Vitaku, E.; Kirschner, M. S.; Schaller, R. D.; Chen, L. X.; Gianneschi, N. C.; Dichtel, W. R. Seeded Growth of Single-Crystal Two-Dimensional Covalent Organic Frameworks. *Science* **2018**, *361*, 52–57.
(51) Li, H.; Chavez, A. D.; Li, H.; Li, H.; Dichtel, W. R.; Bredas, J.-L. Nucleation and Growth of Covalent Organic Frameworks from Solution: The Example of COF-5. *J. Am. Chem. Soc.* **2017**, *139*, 16310–16318.
(52) Yang, L.; Dincă, M. Redox Ladder of Ni_3 Complexes with Closed-Shell, Mono-, and Diradical Triphenylene Units: Molecular Models for Conductive 2D MOFs. *Angew. Chem. Int. Ed.* **2021**, *60*, 23784–23789.
(53) Yang, L.; He, X.; Dincă, M. Triphenylene-Bridged Trinuclear Complexes of Cu: Models for Spin Interactions in Two-Dimensional Electrically Conductive Metal–Organic Frameworks. *J. Am. Chem. Soc.* **2019**, *141*, 10475–10480.
(54) Smith, M. K.; Mirica, K. A. Self-Organized Frameworks on Textiles (SOFT): Conductive Fabrics for Simultaneous Sensing, Capture, and Filtration of Gases. *J. Am. Chem. Soc.* **2017**, *139*, 16759–16767.
(55) Ko, M.; Mendecki, L.; Eagleton, A. M.; Durbin, C. G.; Stolz, R. M.; Meng, Z.; Mirica, K. A. Employing Conductive Metal–Organic Frameworks for Voltammetric Detection of Neurochemicals. *J. Am. Chem. Soc.* **2020**, *142*, 11717–11733.
(56) Ha, D.-G.; Rezaee, M.; Han, Y.; Siddiqui, S. A.; Day, R. W.; Xie, L. S.; Modtland, B. J.; Muller, D. A.; Kong, J.; Kim, P.; Dincă, M.; Baldo, M. A. Large Single Crystals of Two-Dimensional π-Conjugated Metal–Organic Frameworks via Biphasic Solution-Solid Growth. *ACS Cent. Sci.* **2021**, *7*, 104–109.
(57) Rubio-Giménez, V.; Galbiati, M.; Castells-Gil, J.; Almora-Barrios, N.; Navarro-Sánchez, J.; Escorcia-Ariza, G.; Mattera, M.; Arnold, T.; Rawle, J.; Tatay, S.; Coronado, E.; Martí-Gastaldo, C. Bottom-Up Fabrication of Semiconductive Metal-Organic Framework Ultrathin Films. *Adv. Mater.* **2018**, *30*, 1704291.
(58) Cui, J.; Xu, Z. An Electroactive Porous Network from Covalent Metal–Dithiolene Links. *Chem Commun* **2014**, *50*, 3986–3988.
(59) Meng, H.; Han, Y.; Zhou, C.; Jiang, Q.; Shi, X.; Zhan, C.; Zhang, R. Conductive Metal–Organic Frameworks: Design, Synthesis, and Applications. *Small Methods* **2020**, *4*, 2000396.
(60) Jo, Y.-M.; Lim, K.; Yoon, J. W.; Jo, Y. K.; Moon, Y. K.; Jang, H. W.; Lee, J.-H. Visible-Light-Activated Type II Heterojunction in Cu_3(Hexahydroxytriphenylene)$_2$/Fe_2O_3Hybrids for Reversible NO_2 Sensing: Critical Role of π–Π* Transition. *ACS Cent. Sci.* **2021**, *7*, 1176–1182.
(61) Mähringer, A.; Rotter, J. M.; Medina, D. D. Nanostructured and Oriented Metal–Organic Framework Films Enabling Extreme Surface Wetting Properties. *Beilstein J. Nanotechnol.* **2019**, *10*, 1994–2003.
(62) Smith, M. K.; Jensen, K. E.; Pivak, P. A.; Mirica, K. A. Direct Self-Assembly of Conductive Nanorods of Metal–Organic Frameworks into Chemiresistive Devices on Shrinkable Polymer Films. *Chem. Mater.* **2016**, *28*, 5264–5268.

(63) Wu, H.; Zhang, W.; Kandambeth, S.; Shekhah, O.; Eddaoudi, M.; Alshareef, H. N. Conductive Metal–Organic Frameworks Selectively Grown on Laser-Scribed Graphene for Electrochemical Microsupercapacitors. *Adv. Energy Mater.* **2019**, *9*, 1900482.
(64) Wang, S.; Liu, M.; Shi, Y.; Yang, X.; Li, L.; Lu, Q.; Zheng, H.; Feng, S.; Bai, Y.; Zhang, T. Vertically Aligned Conductive Metal-Organic Framework Nanowires Array Composite Fiber as Efficient Solid-Contact for Wearable Potentiometric Sweat Sensing. *Sens. Actuators B Chem.* **2022**, *369*, 132290.
(65) Blum, M.-M.; John, H. Historical Perspective and Modern Applications of Attenuated Total Reflectance - Fourier Transform Infrared Spectroscopy (ATR-FTIR): Modern Applications of ATR-FTIR. *Drug Test. Anal.* **2012**, *4*, 298–302.
(66) Hind, A. R.; Bhargava, S. K.; McKinnon, A. At the Solid/Liquid Interface: FTIR/ATR - the Tool of Choice. **2001**, *93*, 91–114.
(67) Tian, Y.; Xie, L.; Liu, X.; Geng, Y.; Wang, J.; Ma, M. In Situ Synthesis of Self-Supporting Conductive CuCo-Based Bimetal Organic Framework for Sensitive Nonenzymatic Glucose Sensing in Serum and Beverage. *Food Chem.* **2024**, *437*, 137875.
(68) Lu, G.; Zong, B.; Tao, T.; Yang, Y.; Li, Q.; Mao, S. High-Performance $Ni_3(HHTP)_2$ Film-Based Flexible Field-Effect Transistor Gas Sensors. *ACS Sens.* **2024**, *9*, 1916–1926.
(69) Lee, H.; Jeon, S. Polyacrylonitrile Nanofiber Membranes Modified with Ni-Based Conductive Metal Organic Frameworks for Air Filtration and Respiration Monitoring. *ACS Appl. Nano Mater.* **2020**, *3*, 8192–8198.
(70) Li, J.; Huang, Y.; Zhou, Y.; Dong, H.; Wang, H.; Shan, H.; Li, Y.; Xu, M.; Wang, X. Controllable Construction of Two-Dimensional Conductive $M_3(HHTP)_2$ Nanorods for Electrochemical Sensing of Malachite Green in Fish. *ACS Appl. Nano Mater.* **2023**, *6*, 22916–22926.
(71) Ingle, N.; Sayyad, P.; Bodkhe, G.; Mahadik, M.; AL-Gahouari, T.; Shirsat, S.; Shirsat, M. D. ChemFET Sensor: Nanorods of Nickel-Substituted Metal–Organic Framework for Detection of SO_2. *Appl. Phys. A* **2020**, *126*, 723.
(72) Qiao, Y.; Liu, Q.; Lu, S.; Chen, G.; Gao, S.; Lu, W.; Sun, X. High-Performance Non-Enzymatic Glucose Detection: Using a Conductive Ni-MOF as an Electrocatalyst. *J. Mater. Chem. B* **2020**, *8*, 5411–5415.
(73) Mendecki, L.; Mirica, K. A. Conductive Metal–Organic Frameworks as Ion-to-Electron Transducers in Potentiometric Sensors. *ACS Appl. Mater. Interfaces* **2018**, *10*, 19248–19257.
(74) Yang, Y.; Ji, W.; Yin, Y.; Wang, N.; Wu, W.; Zhang, W.; Pei, S.; Liu, T.; Tao, C.; Zheng, B.; Wu, Q.; Li, L. Catalytic Modification of Porous Two-Dimensional Ni-MOFs on Portable Electrochemical Paper-Based Sensors for Glucose and Hydrogen Peroxide Detection. *Biosensors* **2023**, *13*, 508.
(75) Barthram, A. M.; Cleary, R. L.; Kowallick, R.; Ward, M. D. A New Redox-Tunable near-IR Dye Based on a Trinuclear Ruthenium(II) Complex of Hexahydroxytriphenylene. *Chem. Commun.* **1998**, *24*, 2695–2696.
(76) Grange, C. S.; Meijer, A. J. H. M.; Ward, M. D. Trinuclear Ruthenium Dioxolene Complexes Based on the Bridging Ligand Hexahydroxytriphenylene: Electrochemistry, Spectroscopy, and near-Infrared Electrochromic Behaviour Associated with a Reversible Seven-Membered Redox Chain. *Dalton Trans* **2010**, *39*, 200–211.
(77) Seoane, B.; Castellanos, S.; Dikhtiarenko, A.; Kapteijn, F.; Gascon, J. Multi-Scale Crystal Engineering of Metal Organic Frameworks. *Coord. Chem. Rev.* **2016**, *307*, 147–187.

(78) Łuczak, J.; Kroczewska, M.; Baluk, M.; Sowik, J.; Mazierski, P.; Zaleska-Medynska, A. Morphology Control through the Synthesis of Metal-Organic Frameworks. *Adv. Colloid Interface Sci.* **2023**, *314*, 102864.
(79) Lewis, C. S.; Moronta, D.; Terban, M. W.; Wang, L.; Yue, S.; Zhang, C.; Li, Q.; Corrao, A.; Billinge, S. J. L.; Wong, S. S. Synthesis, Characterization, and Growth Mechanism of Motifs of Ultrathin Cobalt-Substituted $NaFeSi_2O_6$ Nanowires. *CrystEngComm* **2018**, *20*, 223–236.
(80) Trindade, F. J.; Damasceno, S.; Otubo, L.; Felez, M. R.; De Florio, D. Z.; Fonseca, F. C.; Ferlauto, A. S. Tuning of Shape, Defects, and Disorder in Lanthanum-Doped Ceria Nanoparticles: Implications for High-Temperature Catalysis. *ACS Appl. Nano Mater.* **2022**, *5*, 8859–8867.
(81) Xu, Y.; Yang, S.; Zhang, G.; Sun, Y.; Gao, D.; Sun, Y. Uniform Hematite α-Fe_2O_3 Nanoparticles: Morphology, Size-Controlled Hydrothermal Synthesis and Formation Mechanism. *Mater. Lett.* **2011**, *65*, 1911–1914.
(82) Khalil, M.; Yu, J.; Liu, N.; Lee, R. L. Hydrothermal Synthesis, Characterization, and Growth Mechanism of Hematite Nanoparticles. *J. Nanoparticle Res.* **2014**, *16*, 2362.
(83) Seki, T.; Chiang, K.-Y.; Yu, C.-C.; Yu, X.; Okuno, M.; Hunger, J.; Nagata, Y.; Bonn, M. The Bending Mode of Water: A Powerful Probe for Hydrogen Bond Structure of Aqueous Systems. *J. Phys. Chem. Lett.* **2020**, *11*, 8459–8469.
(84) Cote, A. P.; Benin, A. I.; Ockwig, N. W.; O'Keeffe, M.; Matzger, A. J.; Yaghi, O. M. Porous, Crystalline, Covalent Organic Frameworks. **2005**, *310*, 1166–1170.
(85) Barreto, W. J.; Ando, R. A.; Santos, P. S.; Silva, W. P. Preparation, UV–Vis, IR, EPR and Resonance Raman Study of Fe, Ni, Co and Zn Dioxolene Complexes. *Spectrochim. Acta. A. Mol. Biomol. Spectrosc.* **2007**, *68*, 612–618.
(86) Leubner, S.; Bengtsson, V. E. G.; Inge, A. K.; Wahiduzzaman, M.; Steinke, F.; Jaworski, A.; Xu, H.; Halis, S.; Rönfeldt, P.; Reinsch, H.; Maurin, G.; Zou, X.; Stock, N. Hexahydroxytriphenylene for the Synthesis of Group 13 MOFs – a New Inorganic Building Unit in a β-Cristobalite Type Structure. *Dalton Trans.* **2020**, *49*, 3088–3092.
(87) Ojani, R.; Raoof, J.-B.; Norouzi, B. An Efficient Sensor for Determination of Concentrated Hydrogen Peroxide Based on Nickel Oxide Modified Carbon Paste Electrode. *Int. J. Electrochem. Sci.* **2012**, *7*, 1852–1863.
(88) Shul'pin, G. B. Alkane Oxygenation with Hydrogen Peroxide Catalysed by Soluble Derivatives of Nickel and Platinum. *J. Chem. Res.* **2002**, *2002*, 351–353.
(89) Smith, B. J.; Dichtel, W. R. Mechanistic Studies of Two-Dimensional Covalent Organic Frameworks Rapidly Polymerized from Initially Homogenous Conditions. *J. Am. Chem. Soc.* **2014**, *136*, 8783–8789.
(90) Debela, T. T.; Yang, M. C.; Hendon, C. H. Ligand-Mediated Hydrogenic Defects in Two-Dimensional Electrically Conductive Metal–Organic Frameworks. *J. Am. Chem. Soc.* **2023**, *145*, 11387–11391.

TOC GRAPHIC

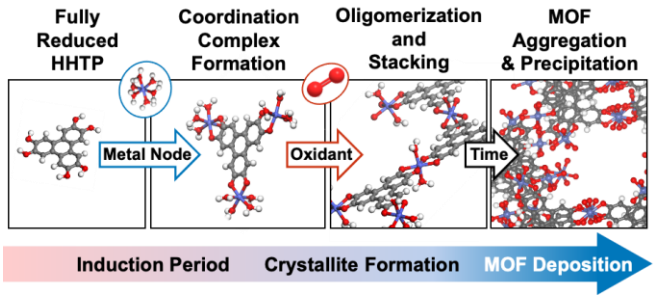

(max 9 cm x 4 cm)